Nonlinear Mixed Modes in Red Giants

The Astrophysical Journal, 873:67 (8pp), 2019 March 1 https://doi.org/10.3847/1538-4357/ab0204

Nonlinear Mixed Modes in Red Giants

Nevin N. Weinberg[1] and Phil Arras[2]
[1] Department of Physics, and Kavli Institute for Astrophysics and Space Research, Massachusetts Institute of Technology, Cambridge, MA 02139, USA
[2] Department of Astronomy, University of Virginia, P.O. Box 400325, Charlottesville, VA 22904-4325, USA
Received 2018 September 5; revised 2019 January 23; accepted 2019 January 24; published 2019 March 5

Abstract

Turbulent motions in the convective envelope of red giants excite a rich spectrum of solar-like oscillation modes. Observations by *CoRoT* and *Kepler* have shown that the mode amplitudes increase dramatically as the stars ascend the red giant branch, i.e., as the frequency of maximum power, $\nu_{\rm max}$, decreases. Most studies nonetheless assume that the modes are well described by the linearized fluid equations. We investigate to what extent the linear approximation is justified as a function of stellar mass M and $\nu_{\rm max}$, focusing on dipole mixed modes with frequency near $\nu_{\rm max}$. A useful measure of a mode's nonlinearity is the product of its radial wavenumber and its radial displacement, $k_r\xi_r$ (i.e., its shear). We show that $k_r\xi_r \propto \nu_{\rm max}^{-9/2}$, implying that the nonlinearity of mixed modes increases significantly as a star evolves. The modes are weakly nonlinear ($k_r\xi_r > 10^{-3}$) for $\nu_{\rm max} \lesssim 150\ \mu$Hz and strongly nonlinear ($k_r\xi_r > 1$) for $\nu_{\rm max} \lesssim 30\ \mu$Hz, with only a mild dependence on M over the range we consider (1.0–2.0 $M_\odot$). A weakly nonlinear mixed mode can excite secondary waves in the stellar core through the parametric instability, resulting in enhanced, but partial, damping of the mode. By contrast, a strongly nonlinear mode breaks as it propagates through the core and is fully damped there. Evaluating the impact of nonlinear effects on observables such as mode amplitudes and linewidths requires large mode network simulations. We plan to carry out such calculations in the future and investigate whether nonlinear damping can explain why some red giants exhibit dipole modes with unusually small amplitudes, known as depressed modes.

Key words: asteroseismology – stars: evolution – stars: interiors – stars: oscillations (including pulsations) – waves

1. Introduction

The detection of solar-like oscillations by the *CoRoT* (Baglin et al. 2006) and *Kepler* (Borucki et al. 2010) space missions has yielded a wealth of information about the internal and global properties of thousands of red giants (see reviews by Chaplin & Miglio 2013; Hekker & Christensen-Dalsgaard 2017). Highlights include powerful scaling relations that connect seismic parameters to fundamental stellar parameters (e.g., mass, radii, and luminosity) and the detection of mixed modes, which behave like acoustic waves in the convective envelope and internal gravity waves in the radiative core. Measurements of mixed-mode period spacings make it possible to distinguish between hydrogen- and helium-burning red giants (Bedding et al. 2011; Mosser et al. 2011; Stello et al. 2013; Mosser et al. 2014) and constrain the core rotation profile (Beck et al. 2012; Deheuvels et al. 2012, 2014; Mosser et al. 2012b).

The propagation and damping of solar-like oscillations is usually described in terms of the linearized fluid equations. This approximation, in which waves propagate without interacting, greatly simplifies the analysis of the wave dynamics. In the Sun, acoustic waves (p-modes) have sufficiently small amplitude that the linear approximation is well justified throughout most of the star (Christensen-Dalsgaard 2002). The exceptions are the uppermost regions of the convective zone and the optically thin region above the photosphere, where the Mach numbers approach one (Kumar & Goldreich 1989). However, since there is very little mass in these regions, nonlinear mode interactions do not contribute significantly to the mode damping (Kumar & Goldreich 1989) and barely modify the mode frequencies and linewidths (Kumar et al. 1994).

In this paper we argue that, unlike the case for main-sequence stars, nonlinear effects may become important as stars ascend the red giant branch (RGB). There are two reasons. First, mode amplitudes are observed to increase as stars ascend the RGB, increasing the size of nonlinear effects. Second, for the case of dipole (angular degree $\ell = 1$) mixed modes, a new type of nonlinear interaction may become important, namely the steepening of the gravity wave near the center. We investigate the onset of three-wave interactions in the weakly nonlinear limit, as well as the strongly nonlinear limit in which the wave may overturn the stratification near the center, causing the wave to break and deposit its energy there.

Throughout the study, we focus on the stability of low-ℓ mixed modes because the observations do not have the spatial resolution to detect modes with $\ell \gtrsim 3$. We are particularly interested in the stability of pressure-dominated mixed modes (p-m modes) since such modes have detectable surface amplitudes and yet propagate deep within the stellar core where nonlinear mode interactions can be important.

Our calculations rely on RGB models constructed with the MESA stellar evolution code (Paxton et al. 2011, 2013, 2015, 2018). We consider models with mass $M = [1.0, 2.0]\ M_\odot$ and $\nu_{\rm max} \simeq [10, 200]\ \mu$Hz, which coincide with the range observed by *CoRoT* and *Kepler*. We find that the nonlinear mode parameters are not especially sensitive to M and therefore focus on representative models with $M = \{1.2, 1.6, 2.0\}$. We find eigenmodes of the stellar models with the GYRE oscillation code (Townsend & Teitler 2013; Townsend et al. 2018), and normalize the spatial eigenfunctions $\boldsymbol{\xi}_a(\boldsymbol{x})$ such that $\omega_a^2 \int d^3x \rho\ |\boldsymbol{\xi}_a|^2 = E_*$, where ω_a is the eigenfrequency and ρ is the density. We express mode energy in units of $E_* \equiv GM^2/R$, where R is the stellar radius.

The paper is organized as follows. In Section 2, we estimate the energy of mixed modes as a function of stellar mass M and position on the RGB, or equivalently $\nu_{\rm max}$, the frequency of maximum power. In Section 3, we calculate the maximum

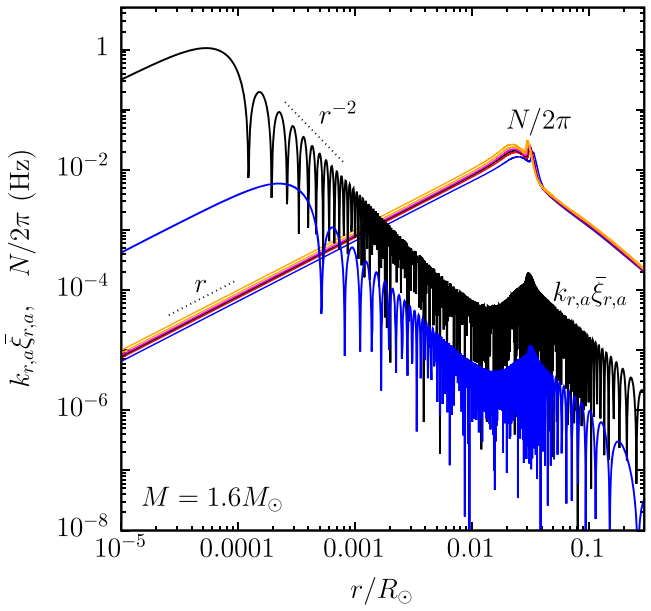

Figure 1. Profiles of $N/2\pi$ and $k_{r,a}\bar{\xi}_{r,a}$ of *p-m* mixed modes (black and blue oscillatory lines) for $M = 1.6\,M_\odot$ RGB models. The six $N/2\pi$ curves are at different evolutionary stages, corresponding to $\nu_{\max} = \{230, 137, 104, 81, 53, 30\}$ μHz from bottom to top. The black (blue) mixed mode is from the $\nu_{\max} = 30$ μHz (104 μHz) model, with $\ell_a = 1$, $\nu_a \simeq \nu_{\max}$ and E_a given by Equation (1).

shear of mixed modes, which provides a measure of their nonlinearity. In Section 4 we consider the weakly nonlinear regime and study the amplitude equations describing nonlinear three-mode interactions. We summarize our results in Section 5 and briefly discuss the possibility that the observed depressed modes are due to nonlinear damping.

2. Energy of Mixed Modes

By characterizing the power excess of ≃1200 *Kepler* red giants, Mosser et al. (2012a) showed that the bolometric oscillation amplitudes on the RGB are ∼10–100 times larger than the Sun's, and increase dramatically as the stars evolve along the RGB (see also Vrard et al. 2018). The amplitudes are larger because the convective motions are especially vigorous in the low density envelope of red giants (see, e.g., Kjeldsen & Bedding 1995; Samadi et al. 2007). Recent 3D hydrodynamical models are broadly consistent with the observations, and find that the mode excitation rate, $\mathcal{P}$, is a strong function of a star's luminosity-to-mass ratio, scaling as $\mathcal{P} \propto (L/M)^{2.6}$ (Samadi et al. 2007, 2012).

The time-averaged linear energy of a solar-like oscillation $E_{a,\rm lin} = \mathcal{P}_a/2\gamma_a = \mathcal{M}_a \mathrm{v}_a^2$, where $\mathcal{P}_a$ is the time-averaged power supplied to the mode by turbulent convection, γ_a is the linear damping rate of the mode, $\mathcal{M}_a = MI_a$ is the mode mass, I_a is the dimensionless mode inertia, and v_a^2 is the mean-squared surface velocity (see, e.g., Belkacem et al. 2006). The linear energy of a *p-m* mode $E_{a,\rm lin} \simeq E_0 = \mathcal{P}_0/2\gamma_0$, where E_0 is the time-averaged linear energy of the neighboring radial mode ($\ell = 0$) of frequency $\nu_0 \simeq \nu_a$, with subscript 0 denoting radial modes. The *p-m* mode and radial mode have nearly equal energy because both are damped primarily in the convective envelope, which implies that their work integrals are nearly equal and therefore $\mathcal{M}_a\gamma_a \simeq \mathcal{M}_0\gamma_0$ (Dupret et al. 2009; Grosjean et al. 2014). Moreover, $\mathcal{M}_a\mathcal{P}_a \simeq \mathcal{M}_0\mathcal{P}_0$ because their structures are nearly the same in the convective envelope, where the driving occurs (Dupret et al. 2009; Benomar et al. 2014; Grosjean et al. 2014).

By fitting the frequency spectra of more than 5000 red giants, Vrard et al. (2018) determine the linewidths $\Gamma_0 = \gamma_0/\pi$ of radial modes with $\nu_0 \simeq \nu_{\max}$ (see also Corsaro et al. 2015; Handberg et al. 2017). They find $\Gamma_0(\nu_{\max}) \approx 0.05$–$0.2$ μHz over the range $M \simeq [0.8, 2.5]M_\odot$ and $\nu_{\max} \simeq [10, 200]$ μHz. Samadi et al. (2012) estimate $\mathcal{P}_0(M, \nu_{\max})$ from their 3D hydrodynamical models of mode excitation in the upper layers of red giants. They find $\mathcal{P}_0(M, \nu_{\max}) = Bx^s$, where $x = (L/L_\odot)(M_\odot/M)$, $B = 4.2^{+1.0}_{-0.8} \times 10^{22}$ erg s^{-1}, and $s = 2.60 \pm 0.08$. Thus,

$$E_{a,\rm lin}(M, \nu_{\max}) \simeq (1.8^{+0.4}_{-0.3}) \times 10^{-16} \times \left(\frac{\beta}{1.5}\right)^2 \left(\frac{\Gamma_0}{0.1\ \mu\mathrm{Hz}}\right)^{-1} \left(\frac{M}{1.5\,M_\odot}\right)^{-3/2} \times \left(\frac{T_{\rm eff}}{4800\ \mathrm{K}}\right)^{8.9\pm0.3} \left(\frac{\nu_{\max}}{100\ \mu\mathrm{Hz}}\right)^{-3.1\mp0.1} \quad (1)$$

(in units of GM^2/R), where $T_{\rm eff}$ is the effective temperature and we used the scaling relations $L \propto R^2T_{\rm eff}^4$ and $\nu_{\max} \propto MR^{-2}T_{\rm eff}^{-1/2}$ with solar reference values of $\nu_{\max,\odot} = 3101$ μHz and $T_{\rm eff,\odot} = 5777$K (Kjeldsen & Bedding 1995; Stello et al. 2009; Huber et al. 2010). We include a correction factor β because Samadi et al. (2012) find that the observed bolometric amplitudes A_0 are ≈1.5 times larger than those predicted by their hydrodynamical models and suggest that it could be due to their models underestimating $\mathcal{P}_0$ by a factor of β^2.

We can also express this result in terms of the bolometric amplitude $A_{a,\rm lin} \simeq A_0 \propto \zeta v_0 \propto \zeta(E_0/\mathcal{M}_0)^{1/2}$, where ζ is a dimensionless coefficient. Samadi et al. (2012) find $\zeta \simeq (0.59 \pm 0.07)x^k$ and $\mathcal{M}_0 = Cy^{-p}$, where $y = \Delta\nu/\Delta\nu_\odot$, $\Delta\nu$ is the large frequency separation, $k = 0.25 \pm 0.05$, $C = 8.0^{+2.8}_{-2.1} \times 10^{24}$ g, and $p = 2.0 \pm 0.1$. This gives

$$A_{a,\rm lin}(M, \nu_{\max}) \simeq (35^{+11}_{-8})\ \mathrm{ppm} \times \left(\frac{\beta}{1.5}\right) \left(\frac{\Gamma_0}{0.1\ \mu\mathrm{Hz}}\right)^{-1/2} \left(\frac{M}{1.5\,M_\odot}\right)^{-0.25\pm0.01} \times \left(\frac{T_{\rm eff}}{4800\ \mathrm{K}}\right)^{5.8\pm0.3} \left(\frac{\nu_{\max}}{100\ \mu\mathrm{Hz}}\right)^{-0.8\pm0.1}, \quad (2)$$

where we used the relation $\Delta\nu \propto (M/R^3)^{1/2}$ and solar reference values $\Delta\nu_\odot = 134.9$ μHz, $A_{0,\odot} = 2.53 \pm 0.11$ ppm, and $v_\odot = 18.5 \pm 1.5$ cm s^{-1} (Samadi et al. 2012). Equation (2) agrees well with the observed bolometric amplitudes measured by Vrard et al. (2018; see their Figure 6).

3. Nonlinearity of Mixed Modes

A dimensionless local measure of nonlinearity is the shear $d\bar{\xi}_{r,a}/dr \simeq k_{r,a}\bar{\xi}_{r,a}$, where $k_{r,a}$ is the radial wavenumber and $\bar{\xi}_{r,a} = E_a^{1/2}\xi_{r,a}$ is the radial displacement in physical units. A perturbation at radius r is strongly nonlinear if $k_{r,a}(r)\bar{\xi}_{r,a}(r) \gtrsim 1$, i.e., if the wavelength is smaller than the displacement, since such a wave is likely to overturn and break rather than continue to propagate (similar to ocean waves approaching the shore). In the core, *p-m* modes are supported by the local buoyancy and $k_{r,a} \simeq \Lambda_a N/\omega_a r \gg R^{-1}$ for $\nu_a \simeq \nu_{\max}$, where $N(r)$ is the Brunt–Väisälä frequency. Since

the wavelengths are small, conservation of Wentzel–Kramers–Brillouin (WKB) flux implies that the radial displacement within the propagation region $\xi_{r,a} \propto r^{-2}$ and the asymptotic eigenmode relations give $|k_r \xi_{r,a}| \approx K \Lambda_a \omega_a^{-1} r^{-2}$, where $K = (E_* C \Delta P_0 / 2\pi^2 \rho)^{1/2}$, $C = N/r$, and $\Delta P_0 = 2\pi^2 \left(\int N d \ln r \right)^{-1}$ (see, e.g., Aerts et al. 2010; Hekker & Christensen-Dalsgaard 2017).

On the RGB, C and K are both nearly constant deep within the core. Figure 1 shows $N(r)$ for an $M = 1.6\,M_\odot$ model at six different ages, corresponding to $\nu_{\max} = \{230, 137, 104, 81, 53, 30\}$ μHz. Although the core contracts with age, we see that for $r \lesssim 0.01\,R_\odot$, the slope of the $N(r)$ profile is nearly constant with radius, with $C = \{4.1, 4.7, 5.0, 5.3, 5.7, 6.4\}$ s$^{-1} R_\odot^{-1}$, respectively. Figure 1 also shows two profiles of $k_{r,a}\bar{\xi}_{r,a}$ for $\ell_a = 1$, $\nu_a \simeq \nu_{\max}$ p-m mixed modes at $\nu_{\max} = 30$ and 104 μHz found with GYRE. The numerical results agree well with the asymptotic expression.

The shear peaks near the mode's inner turning point r_a, which is located where $N(r_a) \simeq C r_a \simeq \omega_a$. For values characteristic of the RGB models ($E_\star \approx 10^{48}$ erg, $\rho \approx 10^5$ g cm^{-3}, $C \approx 5$ s$^{-1} R_\odot^{-1}$, $\Delta P_0 = 100$ s), $r_a \approx 10^{-4} \nu_{a,100}\,R_\odot$ and the maximum shear

$$|k_{r,a}\bar{\xi}_{r,a}|_{\max} \approx 0.01 \Lambda_a \left(\frac{\nu_a}{100\ \mu\text{Hz}} \right)^{-3} \left(\frac{E_a}{10^{-16}} \right)^{1/2} \approx 0.01 \Lambda_a \left(\frac{\beta}{1.5} \right) \left(\frac{\Gamma_0}{0.1\ \mu\text{Hz}} \right)^{-1/2} \left(\frac{M}{1.5\,M_\odot} \right)^{-3/4} \times \left(\frac{T_{\rm eff}}{4800\ \text{K}} \right)^{9/2} \left(\frac{\nu_{\max}}{100\ \mu\text{Hz}} \right)^{-9/2}, \quad (3)$$

where in the second line we plugged in a value of E_a corresponding to the median linear energy $E_{a,\rm lin}$ given by Equation (1). Although the asymptotic eigenmode expressions strictly apply only within the propagation region and not near r_a, they approximate the magnitude and scaling of $|k_{r,a}\bar{\xi}_{r,a}|_{\max}$ very well.

Since the linear energy of mixed modes near $\nu_{\max}$ scales approximately as $E_{a,\rm lin} \propto \nu_a^{-3}$, the maximum shear increases significantly as the star evolves ($|k_{r,a}\bar{\xi}_{r,a}|_{\max} \propto \nu_a^{-9/2}$). Figure 2 shows the numerically calculated maximum shear as a function of $\nu_{\max}$ for p-m modes of the $M = 1.2\,M_\odot$ and $2.0\,M_\odot$ models. To calculate the maximum shear, we use GYRE to find modes with $\ell_a = 1$, $\nu_a \simeq \nu_{\max}$ and from these numerical solutions we compute the maximum of $d\xi_{r,a}/dr \simeq k_{r,a}\xi_{r,a}$ for each mode. We then use Equation (1) to calculate $E_{a,\rm lin}$. We take $\beta = 1.5$, $\Gamma_0 = 0.1$ μHz, and the median values for B and s. The analytic expression for $|k_{r,a}\bar{\xi}_{r,a}|_{\max}$ given by Equation (3) agrees with the numerical result to within a factor of $\approx$2 over the range of M and $\nu_{\max}$ shown in Figure 2. We find that for $50 \lesssim \nu_{\max} \lesssim 150$ μHz, the mixed modes are weakly nonlinear ($0.1 \gtrsim k_{r,a}\bar{\xi}_{r,a} \gtrsim 10^{-3}$). However, for $\nu_{\max} \lesssim 30$ μHz they become strongly nonlinear in the core ($k_{r,a}\bar{\xi}_{r,a} \gtrsim 1$).

Despite the uncertainties in $E_{a,\rm lin}$ (due to uncertainties and observational scatter in the parameters that determine the energy), the steep $\nu_{\max}^{-9/2}$ dependence implies that there is a narrow $\nu_{\max}$ window where the modes transition from weakly nonlinear to strongly nonlinear. A strongly nonlinear mixed mode will overturn the local stratification in the core and break.

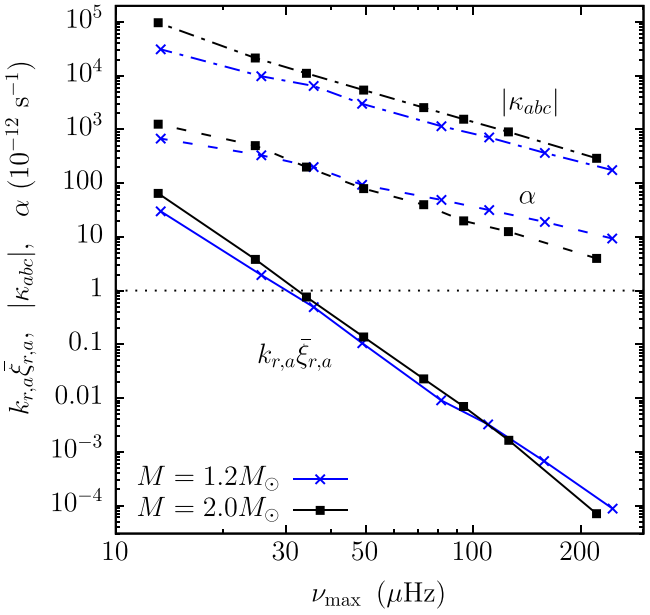

Figure 2. Maximum shear $k_{r,a}\bar{\xi}_{r,a}$ of p-m mixed modes found using GYRE (solid lines) as a function of $\nu_{\max}$ for $M = 1.2\,M_\odot$ (blue curves with crosses) and $2.0\,M_\odot$ (black curves with squares). Also shown are the nonlinear coupling coefficient κ_{abc} (dashed-dotted lines) and linear damping coefficient α (dashed lines; in units of 10^{-12} s^{-1}). The modes are $(\ell_a, \ell_b, \ell_c) = (1, 2, 3)$ with $\nu_a \simeq \nu_{\max}$ and $\nu_b + \nu_c \simeq \nu_a$.

Since they do not reflect at r_a, they are ingoing traveling waves rather than standing waves. This phenomenon can also occur in the context of dynamical tides, where it can lead to rapid, tide-induced orbital evolution (see, e.g., Goodman & Dickson 1998; Barker & Ogilvie 2010; Weinberg et al. 2017). In the present context, the breaking wave is directly observed.

As a star evolves, radiative damping in the core becomes so strong that it can dissipate all the energy from a mode in less than its group travel time across the star. For gravity-dominated mixed modes (g-m modes), this transition occurs at $\nu_{\max} \approx 30$ μHz (Dupret et al. 2009; Grosjean et al. 2014), similar to where wave breaking occurs. However, for p-m modes a significant portion of their energy remains trapped in the envelope and is not lost to radiative damping.

4. Nonlinear Mode Interactions

In the previous section we found that mixed modes are weakly nonlinear over a broad portion of the lower RGB ($\nu_{\max} \approx [50, 200]$ μHz) before becoming strongly nonlinear as the star evolves up the RGB. Weakly nonlinear waves can excite secondary waves through nonlinear mode interactions. Whether a weakly nonlinear primary wave (a parent mode) is unstable to secondary waves (daughter modes) depends on the parent's amplitude, the strength of the nonlinear interactions, and the damping rates and frequency detunings. In this section we assess the stability of weakly nonlinear mixed modes as a function of M and $\nu_{\max}$. We focus on the stability of $\ell = 1$ p-m parent modes with $\nu_a \simeq \nu_{\max}$ coupled to resonant g-m daughter modes.

To account for weakly nonlinear effects, we expand the Lagrangian displacement field as a sum of linear eigenmodes $\boldsymbol{\xi}(\boldsymbol{x}, t) = \sum q_a(t) \boldsymbol{\xi}_a(\boldsymbol{x})$ and keep terms up to $\mathcal{O}(\boldsymbol{\xi}^2)$. The

equation of motion for $\boldsymbol{\xi}(\boldsymbol{x}, t)$ can then be written as a set of coupled, nonlinear amplitude equations (Dziembowski 1982; Kumar & Goodman 1996; Wu & Goldreich 2001; Schenk et al. 2002; Weinberg et al. 2012),

$$\ddot{q}_a + 2\gamma_a \dot{q}_a + \omega_a^2 q_a = \omega_a^2 f_a(t) + \omega_a^2 \sum_b \sum_c \kappa^*_{abc} q^*_b q^*_c, \quad (4)$$

where ω_a and γ_a are the eigenfrequency and linear damping rate of mode a, and the asterisks denote complex conjugation. The linear forcing $f_a(t)$ accounts for the stochastic excitation of mode a due to turbulent motions at the top of the convective envelope. The sum containing the dimensionless three-mode coupling coefficient κ_{abc} accounts for the nonlinear interaction between mode a and other modes b, c. The modes couple only if they satisfy the angular selection rules $|\ell_b - \ell_c| \leqslant \ell_a \leqslant \ell_b + \ell_c$ with $\ell_a + \ell_b + \ell_c$ being even and $m_a + m_b + m_c = 0$ (ℓ is the angular degree and m is the azimuthal order).

We study the stability of weakly nonlinear mixed modes by analyzing Equation (4) for simple three-mode systems. In Section 4.1 we describe our treatment of the linear stochastic forcing $f_a(t)$. In Section 4.2 we present analytic estimates of the stability criterion and daughter growth rates and show example numerical solutions of Equation (4). In Section 4.3 we evaluate the various mode parameters that enter the stability analysis. In Section 4.4 we use these results to determine the stability of mixed modes as a function of M and $\nu_{\rm max}$.

4.1. Linear Stochastic Forcing

The modes are excited by the large number of granules in the upper regions of the convection zone, which each impart small, independent impulses. The most strongly excited modes are those with periods comparable to the eddy turnover time $\omega_a^{-1} \sim \tau_{\rm eddy}$ (Goldreich & Kumar 1988). Since the size of each granule is of the order of a scale height H, there are approximately $(R/H)^2 \gg 1$ granules, and the mean time between impulses is $\Delta t \sim \tau_{\rm eddy}(H/R)^2 \ll \omega_a^{-1}$. Chang & Gough (1998) estimate that in the Sun $(R/H)^2 \sim 10^5$ and $\tau_{\rm eddy} \sim 15$minutes, which implies $\Delta t \sim 10^{-3}$s, i.e., about 10^5 impulses per mode period. In red giants, the impulse rate can be even larger. By contrast, the damping rate of the mode is on a much longer timescale, $\gamma_a^{-1} \gg \tau_{\rm eddy}$.

Similar to previous studies (e.g., Kumar et al. 1988; Chang & Gough 1998), we model the stochastic forcing as a Poisson process involving a random sequence of impulses at times t_j. We assume that the time between consecutive impulses, $\Delta t = t_{j+1} - t_j$, is an independent random variable whose probability density is given by $p(\Delta t) = \mu \exp(-\mu \Delta t)$, where μ is the mean number of impulses per unit time. The mode forcing $f_a(t)$ is the sum of all the individual impulses,

$$f_a(t) = f_{0,a} \sum_j c_j \psi_j(t), \quad (5)$$

where we assume each impulse has a Gaussian time dependence of $\psi_j(t) = \exp[-(t - t_j)^2/2\tau^2]$. Since we expect the correlation time of each impulse to be $\tau \sim \tau_{\rm eddy}$, we set $\omega_a \tau = 1$. The amplitude $c_j = c_{j,r} + i c_{j,i}$ is complex with $c_{j,r}$ and $c_{j,i}$ drawn from a Gaussian probability distribution centered on zero with a standard deviation of one. The constant $f_{0,a}$ sets the overall scale of the mode amplitude. While the discussion above suggests $\mu > 10^5$ per mode period, we find that our numerical results are insensitive to μ as long as we set $\mu \gtrsim 10$ per mode period.

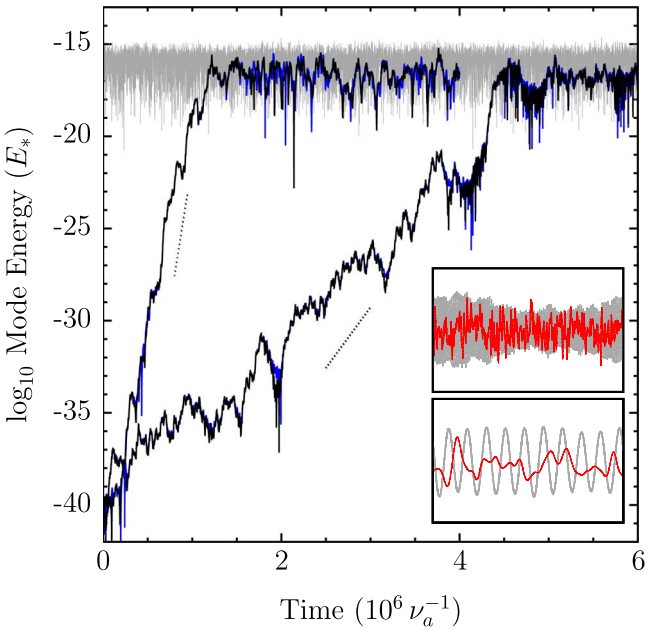

Figure 3. Mode energy as a function of time (main panel) for two examples of a three-mode system involving a stochastically driven parent (gray line) coupled to a resonant daughter pair (black and blue lines) with $f_b = f_c = 0$ and initial energies of $E_b \simeq E_c = 10^{-40}$. The examples differ only by $\gamma_a = (\pi, 2\pi) \times 10^{-4}\nu_a$, with the smaller γ_a corresponding to the more rapidly growing daughter pair. The other parameters are $\mu = 100\nu_a$, $E_{a,\rm lin} \simeq 2 \times 10^{-16}$, $\gamma_b \simeq \gamma_c \simeq 10^{-5}\nu_a$, $\Delta_b \simeq \Delta_c \simeq 10^{-5}\omega_a$, and $\kappa_{abc} = 3 \times 10^3$. The dashed lines show the growth rate scalings given by Equation (9). The insets zoom in on the parent mode and show, on a linear scale, the real parts of $q_a(t)$ (gray lines) and $10 f_a(t)$ (red lines) over durations of $10\nu_a^{-1}$ and $100\nu_a^{-1}$.

One realization of this random process corresponds to a set of t_j and c_j. Each realization, $\mathcal{R}$, will produce a different solution, $q_a^{(\mathcal{R})}(t)$, to Equation (4) for the parent amplitude. The ensemble average, which we denote by angle brackets, corresponds to the average of all these realizations. This ensemble average can be carried out either by averaging many numerical simulations, or in analytic work by directly averaging over the Poisson distribution for the t_j and the Gaussian distribution for the c_j. In addition, single realizations that include very large numbers of events are expected to approximate the ensemble average. Hence even though single realization results are shown in Figure 3, over long timescales we expect the results to be comparable to ensemble averaging.

In the absence of nonlinear coupling, $q_a(t)$ satisfies the equation of a damped linear oscillator forced by a stationary random function for which different events are uncorrelated. The ensemble average of the parent energy, which we denote as $E_{a,\rm lin}$, is

$$E_{a,\rm lin} \equiv \langle |q_a(t)|^2 \rangle \approx (f_{0,a}\omega_a \tau)^2 \left(\frac{\mu}{2\gamma_a}\right). \quad (6)$$

This expression can be understood as follows. Integrating the forcing $\propto f_{0,a}\omega_a$ over the impulse time τ gives an amplitude of $f_{0,a}\omega_a\tau$ for one impulse. Over the damping time γ_a^{-1}, there are μ/γ_a impulses which add randomly, giving the result in Equation (6).

Ensemble averaging products of first order amplitudes requires the autocorrelation function of the forcing. For the daughters, the random forcing function involves the parent amplitude. For our model, the correlation function is approximately

$$\langle q_a^*(t) q_a(t') \rangle \simeq E_{a,\rm lin} e^{-\gamma_a |t-t'|} \cos\left[\omega_a (t-t')\right]. \tag{7}$$

This correlation function oscillates at the parent frequency, and has an exponential dependence with correlation time γ_a^{-1}, the damping time of the parent. The growth rate of the daughters relies on the Fourier transform of this correlation function. We define the power $P_a(\omega)$ to be

$$\begin{aligned} P_a(\omega) &\equiv \mathrm{Re} \int_0^\infty d(t-t') e^{-i\omega(t-t')} \langle q_a^*(t) q_a(t') \rangle \\ &\simeq \frac{E_{a,\rm lin}}{2} \int_0^\infty du \cos[(\omega-\omega_a)u] e^{-\gamma_a u} \\ &\simeq \frac{E_{a,\rm lin}}{2} \left[\frac{\gamma_a}{(\omega-\omega_a)^2 + \gamma_a^2} \right]. \end{aligned} \tag{8}$$

Hence the power is a Lorentzian with damping γ_a and detuning $\omega - \omega_a$ (see, e.g., Christensen-Dalsgaard et al. 1989). We will use this result when describing the nonlinear stability of parent modes in Section 4.2

The two insets in Figure 3 show the real part of $q_a(t)$ and $10 \times f_a(t)$ over a duration of $10\nu_a^{-1}$ and $100\nu_a^{-1}$, where $\nu_a = \omega_a/2\pi$. On such timescales, $q_a(t)$ looks like a sinusoidal oscillation with a slowly varying amplitude. The force varies stochastically on a timescale of $\approx \nu_a^{-1}$ and has a characteristic strength of $|f_a| \ll |q_a|$.

4.2. Nonlinear Stability

Consider a stochastically driven parent mode with $\nu_a \simeq \nu_{\rm max}$ that is coupled to a single, self-coupled daughter mode with a frequency of $\nu_b \simeq \nu_a/2$. Observationally, the distribution of mode energies can be fit by a Gaussian envelope with an FWHM of $\delta\nu_{\rm env} \simeq 0.66(\nu_{\rm max}/100\ \mu\mathrm{Hz})^{0.88}$ (Mosser et al. 2012a). A daughter mode with a frequency of $\nu_b \simeq \nu_a/2 \simeq \nu_{\rm max}/2$ therefore has a linear energy that is only $\sim$1% that of its parent. Thus, to a good approximation we can ignore the daughter's linear forcing and set $f_b = 0$. The amplitude equation then reduces to the stochastic Mathieu equation (when $|q_b| \ll |q_a|$), whose stability has been studied extensively (see, e.g., Stratonovich & Romanovskii 1965; Ariaratnam & Tam 1976; van Kampen 1992; Zhang et al. 1993; Poulin & Flierl 2008). In the regime relevant to mixed modes in red giants, it can be shown that the daughter's average nonlinear growth rate is $s_b \simeq -\gamma_b + 2\omega_b^2 \kappa_{abb}^2 P_a(2\omega_b)$, i.e.,

$$s_b \simeq -\gamma_b + \frac{\omega_b^2 \kappa_{abb}^2 E_{a,\rm lin}}{\gamma_a} \left[1 + \frac{\Delta_b^2}{\gamma_a^2} \right]^{-1}, \tag{9}$$

where $\Delta_b = \omega_a - 2\omega_b$ is the daughter detuning and we assume $\gamma_a \gg \gamma_{b,c}$ (see Sections 4.3.1 and 4.3.2). Thus, the parent and daughter are parametrically unstable ($s_b > 0$) if the parent linear energy, $E_{a,\rm lin}$, is larger than a threshold energy of

$$E_{\rm th} = \frac{\gamma_a \gamma_b}{\kappa_{abb}^2 \omega_b^2} \left[1 + \frac{\Delta_b^2}{\gamma_a^2} \right]. \tag{10}$$

For characteristic parameter values (see Section 4.3)

$$\begin{aligned} E_{\rm th} \simeq 2.5 \times 10^{-16} &\left(\frac{\gamma_a}{10^{-7}\ \mathrm{s}^{-1}} \right) \left(\frac{\gamma_b}{10^{-9}\ \mathrm{s}^{-1}} \right) \\ &\times \left(\frac{\kappa_{abb}}{10^3} \right)^{-2} \left(\frac{\nu_b}{100\ \mu\mathrm{Hz}} \right)^{-2} \left[1 + \frac{\Delta_b^2}{\gamma_a^2} \right]. \end{aligned} \tag{11}$$

To understand the scaling with γ_a, note that at a given $E_{a,\rm lin}$, $P_a(2\omega_b) \propto \gamma_a^{-1}$ provided that $|\Delta_b| \ll \gamma_a$. Thus, as γ_a increases, the parent's power is less concentrated near $\omega_a \simeq 2\omega_b$ and the daughter driving is less effective, resulting in smaller s_b and larger $E_{\rm th}$.

Our estimates above assume that only a single daughter pair ($N = 2$) is parametrically excited. However, in studying tidal flows, Weinberg et al. (2012) found that sets of $N \gg 2$ daughters can be collectively excited (see also Essick & Weinberg 2016), and that the growth rate of collective sets is larger by a factor of N (and $E_{\rm th}$ is smaller by a factor of N). If mixed-mode parents excite collective sets of unstable daughters, then s_b ($E_{\rm th}$) can be significantly larger (smaller) than the above estimates.

In Figure 3 we show two examples of parametrically unstable three-mode systems in which a stochastically driven parent is coupled to a resonant daughter pair with $f_b = f_c = 0$. The examples differ only in the assumed value of γ_a. Although there are two daughter modes rather than a single self-coupled daughter, the daughters are similar ($\gamma_b \simeq \gamma_c$, $\omega_b \simeq \omega_c$). We find that they grow in a stochastic fashion and have an instability threshold and average growth rate that agrees reasonably well with Equations (9) and (10). The stochastic nature of the driving necessarily implies that the growth rates vary rapidly with time, and numerically we find that different realizations only approach the ensemble average over long timescales.

If the parent is driven harmonically rather than stochastically, the daughters satisfy the standard Mathieu equation. They would then be subject to the usual parametric subharmonic instability (PSI), with $s_b \simeq -\gamma_b + 2\omega_b \kappa_{abb} E_{a,\rm lin}^{1/2}$ and $E_{\rm th} \simeq (\gamma_b/2\kappa_{abb}\omega_b)^2$, assuming $|\Delta_b| \ll \gamma_b$ (see, e.g., Dziembowski 1982; Wu & Goldreich 2001). For parameter values relevant to the coupling of mixed modes on the RGB, the stochastic growth rate is smaller than the PSI rate by a factor of $\omega_b \kappa_{abb} E_{a,\rm lin}^{1/2}/2\gamma_a \ll 1$, and the stochastic energy threshold is larger by a factor of $4\gamma_a/\gamma_b \gg 1$. In numerical experiments, we find that if we choose (artificial) parameter values such that $\omega_b \kappa_{abb} E_{a,\rm lin}^{1/2}/2\gamma_a \gtrsim 1$, then the daughter grows at the PSI rate rather than the stochastic rate (the latter now being the larger of the two rates). Indeed, for small enough γ_a we expect to recover the PSI since $P_a(\omega_a)$ is so narrowly peaked that, as far as the resonant daughters are concerned, the parent oscillates harmonically.

4.3. Mode Parameters

4.3.1. γ_a

As described in Section 2, $\gamma_a \simeq \mathcal{M}_0 \gamma_0 / \mathcal{M}_a$ and $\Gamma_0 = \gamma_0/\pi \approx 0.05$–$0.2\ \mu$Hz. For $\ell_a = 1$ p-m modes, we find using GYRE that the inertia ratio is $\mathcal{M}_0/\mathcal{M}_a \simeq 0.1$–$0.5$. The

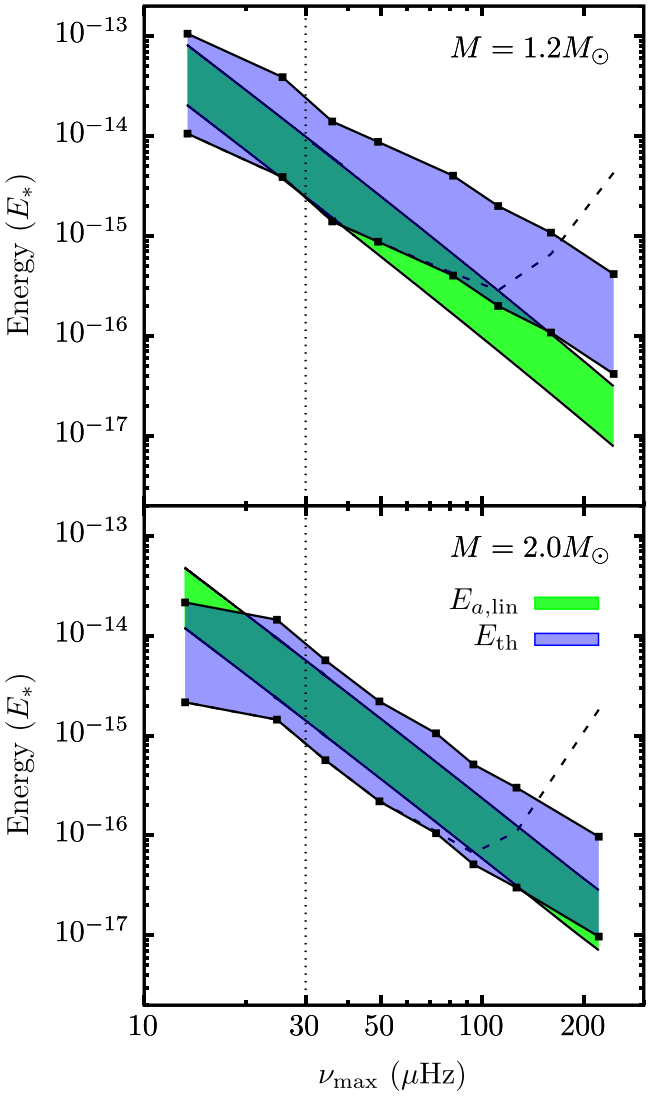

Figure 4. Linear energy $E_{a,\rm lin}$ (green regions) and nonlinear threshold energy $E_{\rm th}$ (blue regions) as a function of $\nu_{\rm max}$ for $M = 1.2\,M_\odot$ (top panel) and $M = 2.0\,M_\odot$ (bottom panel). The factor of 4 range in $E_{a,\rm lin}$ at a given $\nu_{\rm max}$ reflects the observed range of Γ_0; the lower and upper envelopes correspond to $\Gamma_0 = 0.2$ μHz and 0.05 μHz, respectively. The factor of 10 range in $E_{\rm th}$ reflects the range of possible γ_a; the lower and upper envelopes correspond to $\gamma_a = 10^{-8}\,{\rm s}^{-1}$ and $10^{-7}\,{\rm s}^{-1}$, respectively. The $E_{\rm th}$ curves assume $(\ell_a, \ell_b, \ell_c) = (1, 2, 3)$, $\nu_a \simeq \nu_{\rm max}$, and fortuitous detuning of $|\Delta_b| \ll \gamma_a$. The dashed curve shows a portion of $E_{\rm th}$ assuming instead that $|\Delta_b| = \omega_a \ell_b^{-3} n_a^{-2}$. The vertical dotted line indicates the approximate $\nu_{\rm max}$ where mode a becomes strongly nonlinear ($k_{r,a}\bar{\xi}_{r,a} > 1$).

exact value depends on how close a particular *p-m* mode is to an acoustic cavity resonance. Those closest to a resonance are the most *p*-mode-like and have $\mathcal{M}_0/\mathcal{M}_a \simeq 0.3$–$0.5$, while those *p-m* modes on either side of a resonance have $\mathcal{M}_0/\mathcal{M}_a \simeq 0.1$–$0.3$ (Goupil et al. 2013; Deheuvels et al. 2015; Mosser et al. 2015). Thus, we estimate that $10^{-8} \lesssim \gamma_a \lesssim 10^{-7}\,{\rm s}^{-1}$, which agrees well with the available measurements of individual *p-m* mode linewidths (Mosser et al. 2018).

4.3.2. $\gamma_{b,c}$

Since daughter *g-m* modes with $\ell_b \gtrsim 2$ are well trapped in the core, they undergo radiative damping in the core but comparatively little damping in the convective envelope. As a result, they tend to have much smaller damping rates than *p-m* modes as long as $\nu_{\rm max} \gtrsim 30$ μHz (Dupret et al. 2009; Grosjean et al. 2014; Mosser et al. 2018).

We can estimate the contribution of the convective envelope to the damping by computing $\mathcal{M}_0\gamma_0/\mathcal{M}_b$ as in Section 4.3.1. For $\ell_b = 2$ *g-m* modes, we find $\mathcal{M}_0/\mathcal{M}_b \lesssim 10^{-3}$ at $\nu_{\rm max} \simeq 200$ μHz for $M = 1.2M_\odot$ and $M = 2.0M_\odot$; the inertia ratio is even smaller for larger ℓ_b and at smaller $\nu_{\rm max}$ because as the star evolves, the core contracts and the *g-m* modes become even more strongly trapped in the *g*-mode cavity. Thus, for modes with $\ell_b \geqslant 2$, the convective envelope contributes $\lesssim 5 \times 10^{-10}\,{\rm s}^{-1}$ given that $\gamma_0/\pi \approx 0.05$–$0.2$ μHz. As we now describe, this is smaller than the contribution from radiative damping in the core.

Using the non-adiabatic calculations in GYRE, which only account for radiative damping, we find $\gamma_b \approx \alpha\Lambda_b^2\nu_{b,100}^{-2}$, where $\Lambda_b^2 = \ell_b(\ell_b+1)$, $\nu_{b,100} = \nu_b/100$ μHz, and α is a model-dependent constant. The quadratic scaling is a consequence of the short-wavelength of the modes (see Hekker & Christensen-Dalsgaard 2017). Values of $\alpha(M, \nu_{\rm max})$ for $M = 1.2M_\odot$ and $2.0M_\odot$ are shown in Figure 2. We find $0.05 \lesssim \alpha/10^{-10}\,{\rm s}^{-1} \lesssim 10$ over the M and $\nu_{\rm max}$ range of our models. There is a strong dependence on $\nu_{\rm max}$ because as the star evolves, the core contracts and N in the core increases (see Equation (3) in Dupret et al. 2009). The dependence on M is fairly weak and non-monotonic (α increases for $M \lesssim 1.6M_\odot$ and then decreases, like the core density).

For example, a resonant daughter pair with $(\ell_b, \ell_c) = (2, 3)$ coupled to a parent with $\nu_a \simeq \nu_{\rm max} = 100$ μHz has $(\gamma_b, \gamma_c) \simeq (2, 5) \times 10^{-9}\,{\rm s}^{-1}$ (since $\alpha \simeq 10^{-10}\,{\rm s}^{-1}$). For comparison, Grosjean et al. (2014), who account for damping in both the core and envelope, find that their models {E, B, F, G} ($M = \{1.0, 1.5, 1.7, 2.1\}M_\odot$ and $\nu_{\rm max} = \{88, 97, 90, 66\}$ μHz) all yield lifetimes of $\gamma^{-1} \simeq 2000$ days (i.e., $\gamma \simeq 6 \times 10^{-9}\,{\rm s}^{-1}$) for $\ell = 2$ modes with $\nu \simeq \nu_{\rm max}$. They do not show results for modes with $\ell > 2$, but their Figure 4 suggests that such modes might have smaller γ than their $\ell = 2$ modes (since they are even more strongly trapped in the core). Note too that their calculations seem to overestimate the damping rates of radial modes by a factor of $\sim$10 (they find lifetimes of $\gamma_0^{-1} \approx 3$ days whereas the observations by Vrard et al. (2018) suggest $\gamma_0^{-1} \gtrsim 20$ days, i.e., $\Gamma_0 \lesssim 0.2$ μHz).

4.3.3. $\Delta_{b,c}$

The minimum daughter detuning is $|\Delta_b| \approx \omega_a \ell_b^{-3} n_a^{-2}$, where n_a is the radial order of the parent (Wu & Goldreich 2001). One factor of n_a comes from the mean period spacing of mixed modes and the other comes from the number of well-coupled daughters given the width of maximum $|\kappa_{abc}|$ (daughters with $|n_b - n_c| \lesssim n_a$ all have similar κ_{abc}; Kumar & Goodman 1996; Weinberg et al. 2012). The ℓ_b^{-3} dependence (or ℓ_b^{-2} if rotation does not lift the m degeneracy) comes from the freedom in choosing daughters allowed by the angular selection rules. Mixed modes near $\nu_{\rm max}$ have short wavelengths in the core and $n_a \approx \Lambda_a/\nu_a\Delta P_0$ (Hekker & Christensen-Dalsgaard 2017). We find $90 \lesssim \Delta P_0 \lesssim 130$ s for $M = [1.0, 1.8]M_\odot$ and $\nu_{\rm max} = [50, 200]$ μHz (larger $\nu_{\rm max}$ and smaller M have larger ΔP_0). This implies that for $\ell_a = 1$, $\ell_b = 2$, and $\nu_{\rm max} \lesssim 100$ μHz, $|\Delta_b| \lesssim 10^{-5}\omega_a$, which agrees well with eigenmode searches with GYRE. Given the γ_a estimate above, $|\Delta_b| < \gamma_a$ for $\nu_{\rm max} \lesssim 100$ μHz. Thus, the more evolved models always

have daughters with sufficiently small $|\Delta_b|$ that detuning does not limit their growth rate or $E_{\rm th}$ (see Equations (9) and (10)).

4.3.4. κ_{abc}

In order to calculate $\kappa_{abc}(M, \nu_{\rm max})$, we search for eigenmode triplets with GYRE and use the expression for κ_{abc} given in Weinberg et al. (2012; see their (A55)-(A62)). The coupling occurs primarily near the inner turning radius of the parent, deep in the stellar core, since that is where the parent's shear $k_{r,a}\xi_{r,a}$ peaks (see Section 3). Daughters with similar wavenumber $|k_{r,b} - k_{r,c}| \lesssim k_{r,a}$ are spatially resonant with the parent and therefore couple strongly to it. Since deep in the core $N \propto r$, good spatial resonance and small detuning imply $\omega_b/\omega_a \simeq \Lambda_b/(\Lambda_b + \Lambda_c)$, and similarly for ω_c. For a given ℓ_a, we use this condition and the angular selection rules to find resonant daughters that maximize $|\kappa_{abc}|$.

Figure 2 shows the maximum $|\kappa_{abc}|$ for $M = 1.2M_\odot$ and $M = 2.0M_\odot$ as a function of $\nu_{\rm max}$ assuming $\nu_a \simeq \nu_{\rm max}$, resonant daughters, and $(\ell_a, \ell_b, \ell_c) = (1, 2, 3)$. We find $\kappa_{abc} \simeq \kappa_0 \nu_{a,100}^{-2}$, where $\kappa_0 \simeq \{900, 1100, 1400\}$ for $M = \{1.2, 1.6, 2.0\}M_\odot$. To understand the magnitude of κ_0 and the $\nu_{\rm max}^{-2}$ scaling, note that while the exact expression for κ_{abc} is complicated and contains many terms, Weinberg et al. (2012; see their Equation (43)) showed that the dominant terms scale with the parent shear and imply $\kappa_{abc} \approx (T\Delta P_0/2\pi^2)\int N k_{r,a}\xi_{r,a} d\ln r$, where the angular integral is $|T| \approx 0.2$ for low-degree modes. Using the asymptotic relation for $k_{r,a}\xi_{r,a}$ given in Section 3, we find $\kappa_{abc} \approx (\Lambda_a TKC^2\Delta P_0/8\pi^4)\nu_a^{-2}$. Plugging in characteristic values from the stellar models ($E_\star \approx 10^{48}$ erg, $\rho \approx 10^5$ g cm^{-3}, $C \approx 5\ {\rm s}^{-1}R_\odot^{-1}$, $\Delta P_0 = 100$ s) gives $\kappa_{abc} \approx 10^3 \nu_{a,100}^{-2}$ for $(\ell_a, \ell_b, \ell_c) = (1, 2, 3)$, in good agreement with the full κ_{abc} calculation.

4.4. Nonlinear Energy Threshold

From the estimates of the various mode parameters given in Section 4.3, we can calculate the nonlinear energy threshold, $E_{\rm th}(M, \nu_{\rm max})$, and compare it to $E_{a,\rm lin}(M, \nu_{\rm max})$ (see Equations (10) and (1)). Representative results are shown in Figure 4 for $M = 1.2M_\odot$ and $M = 2.0M_\odot$ assuming a mixed-mode parent with $\ell_a = 1$ and $\nu_a \simeq \nu_{\rm max}$. The green region shows the possible range of $E_{a,\rm lin}$ given the observed range of $\Gamma_0 \approx 0.05$–0.2 μHz (Vrard et al. 2018). The additional uncertainty in $E_{a,\rm lin}$ due to the uncertainty in $\mathcal{P}_0$ is not accounted for in the figure, which assumes the median values for B and s and $\beta = 1.5$ (see Samadi et al. 2012). The blue region shows the range of possible $E_{\rm th}$ given the order of magnitude range in possible values of γ_a (Section 4.3.1). It assumes that there are daughter modes with sufficiently small detuning that $|\Delta_b| \ll \gamma_a$. The dashed curve shows $E_{\rm th}$ if instead we adopt the likely value of the minimum detuning $|\Delta_b| = \omega_a \ell_b^{-3} n_a^{-2}$, assuming $\gamma_a = 10^{-8}\ {\rm s}^{-1}$ (Section 4.3.3).

We find that stars with smaller $\nu_{\rm max}$ and larger M are more likely to have an $\ell_a = 1$ p-m mode with energy $E_{a,\rm lin}$ above $E_{\rm th}$. Thus, mixed modes are more likely to be parametrically unstable in more evolved, more massive stars. This is because $E_{a,\rm lin} \propto \nu_{\rm max}^{-3.1}$ whereas $E_{\rm th} \propto \nu_{\rm max}^{-2}$ (approximately). Furthermore, at a given $\nu_{\rm max} \gtrsim 50$ μHz, more massive stars have smaller $\gamma_{b,c}$ (i.e., α) and larger κ_{abc} (see Figure 2). Given the range of plausible values of $E_{a,\rm lin}$ and $E_{\rm th}$, a mixed mode could be unstable out to $\nu_{\rm max} \lesssim 100$ μHz for $M = 1.2M_\odot$ and $\nu_{\rm max} \lesssim 130$ μHz for $M = 2.0M_\odot$. It could be unstable out to even larger $\nu_{\rm max}$ (especially for $M = 2.0M_\odot$) if there are daughters that happen to have especially small detuning of $|\Delta_b| \ll \gamma_a$ or if there are collective sets of unstable daughters (Section 4.2). As shown in Figure 2, the modes become strongly nonlinear for $\nu_{\rm max} \lesssim 30$ μHz and the weakly nonlinear stability calculation is no longer applicable (i.e., to the left of the vertical dotted line in Figure 4).

5. Discussion

The amplitudes of mixed modes increase dramatically as a star evolves up the RGB (as $\nu_{\rm max}$ decreases). The maximum shear of the modes $k_r\bar{\xi}_r$ provides a measure of their nonlinearity. By calibrating to the observed bolometric amplitudes, we showed that the maximum shear $k_r\bar{\xi}_r \propto \nu_{\rm max}^{-9/2}$. Thus, the nonlinearity increases rapidly with decreasing $\nu_{\rm max}$. We found that the modes are weakly nonlinear ($k_r\bar{\xi}_r \approx 10^{-3}$) by $\nu_{\rm max} \approx 150$ μHz and strongly nonlinear ($k_r\bar{\xi}_r \approx 1$) by $\nu_{\rm max} \approx 30$ μHz, nearly independent of M.

As a mixed mode propagates through the core, its shear increases as $k_r\bar{\xi}_r \propto r^{-2}$, reaching a peak near the inner turning point at $r \approx 10^{-4}R_\odot(\nu_{\rm max}/100\ \mu{\rm Hz})$. A strongly nonlinear wave will break and deposit all of its energy and angular momentum as it approaches the turning point. By contrast, a weakly nonlinear wave will, if unstable, excite secondary waves within the core, but only lose a portion of its energy and angular momentum before reflecting at the turning point and propagating back outward. Although we defer a study of the observational consequences of these effects to future work, strongly nonlinear waves likely have reduced amplitudes and broadened linewidths. To a lesser extent, the same might be true of weakly nonlinear waves, although here the calculation is more involved as it depends on the details of the nonlinear saturation by secondary waves. A full understanding likely requires a large mode network calculation of the type carried out in the context of neutron star r-mode instabilities (Arras et al. 2003; Brink et al. 2005; Bondarescu et al. 2009) and dynamical tides in hot-Jupiter systems (Essick & Weinberg 2016).

Interestingly, some red giants exhibit dipole modes with unexpectedly low amplitudes, known as depressed modes (Mosser et al. 2012a, 2017; García et al. 2014; Stello et al. 2016a). Although the prevalence of depressed modes depends on M and $\nu_{\rm max}$, these two parameters alone do not predict whether a star's dipole modes are depressed. This suggests that an additional stellar property plays a role. Fuller et al. (2015) proposed that some red giants have strong internal magnetic fields that scatter and trap oscillation-mode energy within the core (the magnetic greenhouse effect). Stello et al. (2016a) find that this mechanism can account for the lack of depressed modes of higher angular degrees (quadrupole and octupole). However, Mosser et al. (2017) measure the visibilities of depressed modes and find that they are not fully damped in the core, contrary to the predictions of the magnetic greenhouse effect.

Since weakly nonlinear, unstable mixed modes are only partially damped in the core, perhaps the observations by Mosser et al. (2017) indicate that depressed modes are a consequence of weakly nonlinear effects rather than magnetic effects. Given that mixed modes lie near the parametric instability threshold over a large range of $\nu_{\rm max}$ (see Figure 4),

their amplitudes may be sensitive to details of the individual mode parameters (e.g., mode linewidths, daughter detunings, coupling coefficients) and the complicated, time-dependent nonlinear mode dynamics. This could explain why depressed modes are found to occur over a large range of $\nu_{\rm max}$ and yet two otherwise similar stars (similar M and $\nu_{\rm max}$) might not both exhibit depressed modes. We found that higher mass stars are more likely to be above the parametric instability threshold for $\nu_{\rm max} \gtrsim 50\ \mu$Hz (compare the top and bottom panels of Figure 4), which is also consistent with observations (Stello et al. 2016b).

Since the nonlinear interactions occur within the core, the degree of amplitude attenuation will depend on the fraction of mode energy that gets transmitted from the acoustic cavity, where the modes are excited, into the g-mode cavity (similar to the magnetic greenhouse effect). Even if a mode is damped in the core by nonlinearities, the amplitude attenuation at the surface will be small if the transmitted fraction is small. This might explain why the visibility of depressed modes increases as $\nu_{\rm max}$ decreases and as the angular degree ℓ increases (Mosser et al. 2012a, 2017; Stello et al. 2016a). Mode network calculations are needed in order to assess this explanation.

This work was supported in part by NASA ATP grant NNX14AB40G. We thank the referee for valuable comments on the manuscript.

Software: `MESA` (Paxton et al. 2011, 2013, 2015, 2018, http://mesa.sourceforge.net), `GYRE` (Townsend & Teitler 2013; Townsend et al. 2018, https://bitbucket.org/rhdtownsend/gyre/wiki/Home).

ORCID iDs

Nevin N. Weinberg https://orcid.org/0000-0001-9194-2084
Phil Arras https://orcid.org/0000-0001-5611-1349

References

Aerts, C., Christensen-Dalsgaard, J., & Kurtz, D. W. 2010, Asteroseismology (Berlin: Springer)
Ariaratnam, S. T., & Tam, D. S. F. 1976, ZaMM, 56, 449
Arras, P., Flanagan, E. E., Morsink, S. M., et al. 2003, ApJ, 591, 1129
Baglin, A., Auvergne, M., Barge, P., et al. 2006, ESA Special Publication 1306, The CoRoT Mission Pre-Launch Status-Stellar Seismology and Planet Finding, ed. M. Fridlund et al. (Paris: ESA), 33
Barker, A. J., & Ogilvie, G. I. 2010, MNRAS, 404, 1849
Beck, P. G., Montalban, J., Kallinger, T., et al. 2012, Natur, 481, 55
Bedding, T. R., Mosser, B., Huber, D., et al. 2011, Natur, 471, 608
Belkacem, K., Samadi, R., Goupil, M. J., Kupka, F., & Baudin, F. 2006, A&A, 460, 183
Benomar, O., Belkacem, K., Bedding, T. R., et al. 2014, ApJL, 781, L29
Bondarescu, R., Teukolsky, S. A., & Wasserman, I. 2009, PhRvD, 79, 104003
Borucki, W. J., Koch, D., Basri, G., et al. 2010, Sci, 327, 977
Brink, J., Teukolsky, S. A., & Wasserman, I. 2005, PhRvD, 71, 064029
Chang, H.-Y., & Gough, D. O. 1998, SoPh, 181, 251
Chaplin, W. J., & Miglio, A. 2013, ARA&A, 51, 353
Christensen-Dalsgaard, J. 2002, RvMP, 74, 1073
Christensen-Dalsgaard, J., Gough, D. O., & Libbrecht, K. G. 1989, ApJL, 341, L103
Corsaro, E., De Ridder, J., & García, R. A. 2015, A&A, 579, A83
Deheuvels, S., Ballot, J., Beck, P. G., et al. 2015, A&A, 580, A96
Deheuvels, S., Doğan, G., Goupil, M. J., et al. 2014, A&A, 564, A27
Deheuvels, S., García, R. A., Chaplin, W. J., et al. 2012, ApJ, 756, 19
Dupret, M.-A., Belkacem, K., Samadi, R., et al. 2009, A&A, 506, 57
Dziembowski, W. 1982, AcA, 32, 147
Essick, R., & Weinberg, N. N. 2016, ApJ, 816, 18
Fuller, J., Cantiello, M., Stello, D., Garcia, R. A., & Bildsten, L. 2015, Sci, 350, 423
García, R. A., Pérez Hernández, F., Benomar, O., et al. 2014, A&A, 563, A84
Goldreich, P., & Kumar, P. 1988, ApJ, 326, 462
Goodman, J., & Dickson, E. S. 1998, ApJ, 507, 938
Goupil, M. J., Mosser, B., Marques, J. P., et al. 2013, A&A, 549, A75
Grosjean, M., Dupret, M.-A., Belkacem, K., et al. 2014, A&A, 572, A11
Handberg, R., Brogaard, K., Miglio, A., et al. 2017, MNRAS, 472, 979
Hekker, S., & Christensen-Dalsgaard, J. 2017, A&AR, 25, 1
Huber, D., Bedding, T. R., Stello, D., et al. 2010, ApJ, 723, 1607
Kjeldsen, H., & Bedding, T. R. 1995, A&A, 293, 87
Kumar, P., Franklin, J., & Goldreich, P. 1988, ApJ, 328, 879
Kumar, P., & Goldreich, P. 1989, ApJ, 342, 558
Kumar, P., Goldreich, P., & Kerswell, R. 1994, ApJ, 427, 483
Kumar, P., & Goodman, J. 1996, ApJ, 466, 946
Mosser, B., Barban, C., Montalbán, J., et al. 2011, A&A, 532, A86
Mosser, B., Belkacem, K., Pinçon, C., et al. 2017, A&A, 598, A62
Mosser, B., Benomar, O., Belkacem, K., et al. 2014, A&A, 572, L5
Mosser, B., Elsworth, Y., Hekker, S., et al. 2012a, A&A, 537, A30
Mosser, B., Gehan, C., Belkacem, K., et al. 2018, A&A, 618, A109
Mosser, B., Goupil, M. J., Belkacem, K., et al. 2012b, A&A, 548, A10
Mosser, B., Vrard, M., Belkacem, K., Deheuvels, S., & Goupil, M. J. 2015, A&A, 584, A50
Paxton, B., Bildsten, L., Dotter, A., et al. 2011, ApJS, 192, 3
Paxton, B., Cantiello, M., Arras, P., et al. 2013, ApJS, 208, 4
Paxton, B., Marchant, P., Schwab, J., et al. 2015, ApJS, 220, 15
Paxton, B., Schwab, J., Bauer, E. B., et al. 2018, ApJS, 234, 34
Poulin, F. J., & Flierl, G. R. 2008, RSPSA, 464, 1885
Samadi, R., Belkacem, K., Dupret, M. A., et al. 2012, A&A, 543, A120
Samadi, R., Georgobiani, D., Trampedach, R., et al. 2007, A&A, 463, 297
Schenk, A. K., Arras, P., Flanagan, É. É., Teukolsky, S. A., & Wasserman, I. 2002, PhRvD, 65, 024001
Stello, D., Cantiello, M., Fuller, J., et al. 2016b, Natur, 529, 364
Stello, D., Cantiello, M., Fuller, J., Garcia, R. A., & Huber, D. 2016a, PASA, 33, e011
Stello, D., Chaplin, W. J., Basu, S., Elsworth, Y., & Bedding, T. R. 2009, MNRAS, 400, L80
Stello, D., Huber, D., Bedding, T. R., et al. 2013, ApJL, 765, L41
Stratonovich, R. L., & Romanovskii, Y. M. 1965, in Non-Linear Transformations of Stochastic Processes, ed. P. Kuznetsov, R. Stratonovich, & V. Tikhonov (Pergamon), 327
Townsend, R. H. D., Goldstein, J., & Zweibel, E. G. 2018, MNRAS, 475, 879
Townsend, R. H. D., & Teitler, S. A. 2013, MNRAS, 435, 3406
van Kampen, N. G. 1992, Stochastic Processes in Physics and Chemistry Publisher (Amsterdam: Elsevier)
Vrard, M., Kallinger, T., Mosser, B., et al. 2018, A&A, 616, A94
Weinberg, N. N., Arras, P., Quataert, E., & Burkart, J. 2012, ApJ, 751, 136
Weinberg, N. N., Sun, M., Arras, P., & Essick, R. 2017, ApJL, 849, L11
Wu, Y., & Goldreich, P. 2001, ApJ, 546, 469
Zhang, W., Casademunt, J., & Viñals, J. 1993, PhFlA, 5, 3147